Mars 1064-nm Spectral Radiance Measurements from the Receiver Noise Response of the Mars Orbiter Laser Altimeter

(Revision 7)

Xiaoli Sun *
Gregory A. Neumann †
James B. Abshire ‡
Maria T. Zuber §

February 28, 2005

Abstract

The Mars Orbiter Laser Altimeter not only provides surface topography from the laser pulse time-of-flight, but also two radiometric measurements, the active measurement of transmitted and reflected laser pulse energy, and the passive measurement of reflected solar illumination. The passive radiometry measurement is accomplished in a novel fashion by monitoring the noise density at the output of the photodetector and solving for the amount of background light. The passive radiometry measurements provide images of Mars at 1064-nm wavelength over a 2 nm bandwidth with sub-km spatial resolution and with 2% or better precision under full illumination. We describe in this paper the principle of operation, the receiver mathematical model, its calibration, and performance assessment from sample measurement data.

---

*NASA Goddard Space Flight Center, Code 694, Laser Remote Sensing Branch, Greenbelt, MD 20771, USA (telephone: 301-614-6732, e-mail: xiaoli.sun-1@nasa.gov)

†Department of Earth, Atmospheric and Planetary Sciences, Massachusetts Institute of Technology, 54-518, Cambridge, MA 02139-4307, USA, also NASA GSFC, Code 697, Greenbelt MD 20771

‡NASA Goddard Space Flight Center, Code 690, Greenbelt, MD 20771, USA

§Department of Earth, Atmospheric and Planetary Sciences, Massachusetts Institute of Technology, 54-518, Cambridge, MA 02139-4307, USA

1 Introduction

The Mars Orbiter Laser Altimeter (MOLA) [1, 2, 3, 4] on board the Mars Global Surveyor (MGS) spacecraft [5, 6] is primarily a laser pulse time-of-flight ranger that measures surface topography. It has produced a high precision topographic map of Mars with 670 million individual laser shots over a period of more than one Mars year [7]. MOLA also provides two radiometric measurements, (a) the ratio of the transmitted to the echo pulse energies and (b) the background light onto the photodetector. The former, which we refer to as active radiometry, measures the reflectance to laser pulses at zero phase angle. The latter, which we refer to as passive radiometry, measures the reflectance to incident sunlight. The MOLA receiver design and calibration for the laser pulse time-of-flight and active radiometry measurements are described in [2]. This paper describes the receiver model and performance analysis for passive radiometry measurements.

The MOLA passive radiometry measurement is accomplished by dynamically adjusting the receiver detection threshold based on the false alarm rate. The false alarm rate, which is the number of threshold crossings per unit time due to detector dark noise and background light, is registered by a counter and used to adjust the detection threshold to maintain a nearly constant false alarm rate. The detection threshold level thereby tracks the background light and allows the receiver to operate at maximum sensitivity under a prescribed false detection probability. Conversely, the false alarm rate and threshold level can be used to solve for the amount of background light entering the detector. The MOLA receiver thereby provides a passive radiometric measurement at a 1064-nm wavelength in a 2-nm-wide bandwidth. In continuous operation, it functions as a single pixel camera, detecting variations in the brightness of Mars with high precision.

2 MOLA Receiver and Solar Background Radiance

The MGS spacecraft orbits Mars in a near-polar, sun-synchronous, near-circular orbit at 400-km mean altitude, with MOLA oriented toward the planet surface along with other payload instruments. The MOLA receiver field of view is co-aligned with the laser beam and covers an area larger than the laser beam footprint. The MOLA telescope sees not only the laser spot but also sunlight scattered off the Mars surface and atmosphere within the receiver field of view. The former is pulsed and gated within a short interval while the latter is continuous and causes the detector noise to rise whenever MGS is on the sunlit side of the planet. Figure 1 shows a simplified diagram of the MOLA measurement configuration and light paths to the receiver.

The background light power P_o incident on the MOLA detector can be written as

$$P_o = I_{Mars}\, \Delta\lambda\, \eta_{rcvr}\, \pi \left(\frac{\theta_{FOV}}{2}\right)^2 A_{tel} \tag{1}$$

where I_{Mars} is the Mars radiance in watts per unit area, unit bandwidth, and unit solid angle subtended by the MOLA receiver, $\Delta\lambda$ is the receiver optical bandwidth, η_{rcvr} is the receiver optics transmission, θ_{FOV} is the receiver field of view, and A_{tel} is the receiver telescope aperture area. Once the background light power is determined, the radiance of Mars can be obtained from the above equation.

Figure 2 shows how the MOLA false alarm rate varied with the detection threshold for different background light levels during a special test on 13 September 2001. As MGS orbited Mars from night into daylight, the detection threshold level was varied and the false alarm rate was monitored. These data show that the false alarm rate, as a function of threshold level, always increases as the background light increases. There is clearly a unique value of background light power for a given false alarm rate and threshold level. The prelaunch dark noise data is also plotted for comparison.

The radiance measurements are usually expressed in terms of the radiance factor, or 'I/F', which is defined as ratio of the measured radiance to that of an ideal diffusive surface in vacuum with 100% reflectance under the same solar illumination. An ideal diffusive surface scatters the incident light uniformly into 2π steradians, and the radiance at any observation angle can be written as $I_0\, cos(\theta_s)/\pi$, where I_0 is the solar irradiance in W $m^{-2}\mu m^{-1}$ and θ_s is the solar incidence or zenith angle. The radiance factor can be written as

$$I/F = \frac{\pi I_{Mars}}{I_0\, cos(\theta_s)} \tag{2}$$

The solar irradiance is well known and has varied by only 0.5% over the past 100 years [8]. The solar irradiance at 1064-nm wavelength is 647 mW m^{-2} nm^{-1} at 1 AU [9], or 279 mW m^{-2} nm^{-1} at Mars' mean solar distance. Due to the eccentricity of Mars' orbit (e=0.0934), the above solar irradiance needs be scaled by the Mars solar distance squared, and varies from 82% to 122% of its mean value during a Mars year. The phase angle, the angle between the light source and the observer line of sight, varies as the spacecraft orbits the planet and can be calculated from the spacecraft attitude and navigation data. Note that the observed Mars radiance consists of transmitted surface reflections and backscattered sunlight by the atmosphere. The two can be separated if the atmosphere backscattering coefficients can be determined via other independent measurement, such as those described in [10].

MOLA also measures the apparent surface reflectance from the ratio of the transmitted to the reflected laser pulse energies. The apparent surface reflectance here is defined as the product of the two-way atmosphere transmission and surface reflectance. As depicted in Figure 1, the apparent surface reflectance is always measured with the laser light source and the observer at zero phase angle, and is subject to opposition enhancement [11]. The ratio of the apparent surface reflectance to the laser pulses to the radiance factor from the passive radiometry measurement may help to determine the atmospheric backscatter to extinction ratio.

The sampling rate of the radiometry measurement is determined by the integration time of the noise threshold crossing or false alarm measurement. Noise triggers are monitored continuously with little dead time. During MOLA ranging operations, the integration time was 1 s. MOLA operated in this mode during the Aerobraking and Mapping mission phases spanning two martian years (Table 1) [6]. During the MGS Extended Mission, after achieving all of its scientific measurement objectives, MOLA's on-board clock oscillator ceased to operate, ending ranging operation. MOLA was then configured to an enhanced passive radiometry measurement mode and continues to operate to this date. In this mode the noise counter readings are updated in the telemetry at a much higher rate, with the integration time set to 0.125 seconds. The threshold levels are lowered so that the false alarm rate is maintained at a higher value, to reduce random counting error over the shorter integration interval. MOLA has operated nearly continuously in the enhanced passive radiometer mode since 10 October 2001. At 400-km orbital altitude the detector field of view covers a $\sim$340-m-diameter circle on Mars' surface. At the MGS ground track speed of 3km/s, a 0.125-second sampling interval corresponds to an along-track distance of 375 m, which when convolved with the receiver field-of-view (FOV) gives a spatial resolution of $\sim$0.5 km. The cross-track resolution depends on the total number of tracks used in forming the image. The MGS orbital period is about 1 hour 58 minutes, and there are 8400 tracks over a Martian year with a track spacing of 3 km at the equator.

3 Converting False Alarm Rates to Background Light Power

A simplified block diagram of the MOLA receiver is shown in Figure 3. Details on MOLA laser ranging and active radiometry measurement have been previously documented in [1, 2, 7]. The subsystems that collectively perform the passive radiometry measurement consist of the detector, postamplifier, lowpass filters, threshold comparators, and the counters that monitor the false alarm rates. Table 2 gives instrument parameters pertinent to the passive radiometry measurements. Note that the receiver does not directly measure the continuous photocurrent as in a conventional radiometer, because the received signal is AC coupled between the detector and the postamplifier. Instead, it measures the density of the shot noise resulted from the detected photons of the background light.

As in a conventional radar, the MOLA receiver dynamically adjusts its detection threshold according to the so-called Neymann-Pearson detection criterion [12], in which the detection threshold is set as low as possible while keeping the average false alarm rate below a predetermined value. False alarms are caused by both the inherent detector dark noise and the quantum noise from the background light onto the detector. The false alarm rate is determined by the probability density function of the total noise and the detection threshold. Since the detector dark noise is known from the preflight test data, the false alarm rate is solely a function of the background light power and the detection threshold. We now show how the background light power can be determined uniquely from any given false alarm rate and detection threshold.

The average number false alarms expected from the MOLA receiver within a counting gate interval can be written as

$$N_{fa} = \frac{T_g}{T_{fa}}, \tag{3}$$

where T_g is the gate interval and T_{fa} is the average time between adjacent false alarm events. The average rate of false alarms, T_{fa}^{-1}, is related to the probability of false alarm at a given time as [12, p.31]

$$p_{fa} = \frac{\tau_W}{T_{fa}}. \tag{4}$$

Here τ_W is the width of a noise pulse above the detection threshold and can be approximated as $\tau_W \approx 1/BW_{3dB}$, where BW_{3dB} is the receiver bandwidth at the -3dB response point ($1/\sqrt{2}$ in signal amplitude). For bandwidth-limited white noise, the occurrences of false alarms are statistically independent and the number of false alarms over a given time interval follows a Poisson distribution.

The probability of a false alarm occurring at a fixed time can be written as

$$p_{fa} = \int_{y_t}^{\infty} p(y)dy, \tag{5}$$

where $p(y)$ is the probability density function (p.d.f.) of the instantaneous noise.

The noise from the MOLA detector is the sum of the photodetector shot noise and the preamplifier noise, which are statistically independent and have different distributions. The p.d.f. of the total noise can be written as the convolution of the p.d.f.'s of the preamplifier circuit noise, $p_c(x)$, and that of the photodetector shot noise, $p_d(x)$, as

$$p(y) = \int_{-\infty}^{\infty} p_c(y-x)p_d(x)dx. \tag{6}$$

For convenience, we define the integration variables, x, y, in units of the number of equivalent photoelectrons at the input to the preamplifier within the receiver integration time.

MOLA uses a silicon avalanche photodiode (APD) as the photodetector. The p.d.f. of the detector noise can be approximated as [13]

$$p_d(x) = \frac{1}{(2\pi G^2 F\bar{n}_e)^{1/2}\left[1+\frac{(x-G\bar{n}_e)(F-1)}{GF\bar{n}_e}\right]^{3/2}} \cdot e^{\left\{\frac{-(x-G\bar{n}_e)^2}{2G^2F\bar{n}_e\left[1+\frac{(x-G\bar{n}_e)(F-1)}{GF\bar{n}_e}\right]}\right\}}, \tag{7}$$

where G is the average APD gain, F is the excess noise factor, and $\bar{n}_e$ is the average number of the detected photons, or the primary photoelectrons, over the integration interval. The excess noise factor can be calculated as [13]

$$F = k_{eff}G + \left(2 - \frac{1}{G}\right)(1 - k_{eff}), \tag{8}$$

with k_{eff} the ratio of the ionization coefficients of holes and electrons in the APD. The mean and standard deviation of the APD output are given by [13]

$$\bar{x} = G\bar{n}_e \tag{9}$$

$$\sigma_d^2 = FG^2\bar{n}_e. \tag{10}$$

The average number of primary photoelectrons is given by

$$\bar{n}_e = \left[\frac{\eta_{APD}P_o}{hc/\lambda} + \frac{I_{db}}{q}\right]\tau_n, \tag{11}$$

where η_{APD} is the APD quantum efficiency, P_o is the received optical power, h is Planck's constant, c is the speed of light, λ is the wavelength, I_{db} is the APD bulk leakage (dark) current, q is the electron charge, and τ_n is the equivalent receiver noise integration time.

The other source of noise in the receiver is the preamplifier noise, which can be modeled as a zero-mean, Gaussian random variable. The standard deviation of the preamplifier noise can be estimated more easily from the frequency domain using the spectral noise density, which can be directly measured. The total noise variance can be obtained by integrating the noise spectrum over the noise bandwidth. For an ideal integrator, the integration time is related to the one-sided noise bandwidth, BW_n, as

$$\tau_n = \frac{1}{2BW_n}. \tag{12}$$

The filters in the MOLA receiver are not ideal integrators and their frequency responses can be approximated as 5-pole Bessel lowpass filters. The noise bandwidth is related to the 3-dB bandwidth by $BW_n = 1.04 \times BW_{3dB}$ using the definition of the noise integration time in Eq.(12). The standard deviation of the integrated noise can be written as

$$\sigma_c^2 = \left(I_c^2 + 2qI_{ds}\right)BW_n\left(\frac{\tau_n}{q}\right)^2 = \left[\frac{I_c^2}{2q^2} + \frac{I_{ds}}{q}\right]\tau_n, \tag{13}$$

with I_c^2 the one-sided preamplifier input noise spectral density in A^2/Hz and I_{ds} is the APD surface leakage current in amperes.

Substituting Eq.'s (6), (7), (9), and (10) into (5), exchanging the order of the double integrals, and using the standard complementary error function $erfc(u) = \frac{2}{\sqrt{\pi}}\int_u^\infty e^{-t^2}dt$, Eq.(5) can be rewritten as

$$p_{fa} = \int_{-\infty}^{\infty}\frac{1}{2}erfc\left(\frac{y_t - x}{\sqrt{2}\sigma_c}\right)\frac{exp\left\{\frac{-(x-\bar{x})^2}{2\sigma_d^2\left[1+\frac{(x-\bar{x})(F-1)G}{\sigma_d^2}\right]}\right\}}{(2\pi\sigma_d^2)^{1/2}\left[1+\frac{(x-\bar{x})(F-1)G}{\sigma_d^2}\right]^{3/2}}dx. \tag{14}$$

The average number of false alarms in a given interval can be obtained by substituting Eq.'s (4) and (14) into (3). All the parameters in the above equations are constant except for $\bar{x}$ and σ_d, which are functions of the received optical power defined in Eq.'s (9), (10) and (11).

Since the number of false alarms, the threshold level, and the received optical power are all monotonic functions of each other, a solution to any one of them given the other two is unique. Numerical methods can be used to solve Eq. (5) for the background light power as a function of the false alarm rate and the threshold level, which we denote as $f(N_{fa}, v_{th})$. Once the received optical power is found, the Mars radiance factor can be obtained from Eq.(1).

4 Calibration

The calibration of the passive radiometry measurement was carried out using data from prelaunch testing, in which the false alarm rates were measured as a function of the threshold level under a set of known background light levels simulated by the ground support equipment (GSE). The false alarm rates and the comparator threshold voltage levels are contained in the telemetry. The threshold used in Eq.(14) can be scaled from the comparator threshold voltages in the telemetry, v_{th}, as,

$$y_{th} = \left(\tau_n \frac{\eta_d G}{hc/\lambda} \frac{a_{thre}}{R_{det}} \right) v_{th}, \tag{15}$$

where R_{det} is the detector responsivity in V W^{-1} and a_{thre} is the scaling factor from the detector assembly output to the comparator input of the appropriate channel. Other MOLA instrument parameters relevant for the passive radiometry measurement are given in Table 2.

Figure 4 shows a plot of the calculated noise count rate as a function of the threshold level for several values of background light level along with measurements taken during prelaunch testing. Three receiver parameter values were refined from those given in [2] in order to optimize the fit between the theory and the measurements. These parameter values had little effect on MOLA ranging performance estimates in [2] but they had a significant effect in determining the exact shape of the noise probability density function on which the passive radiometry measurement depends. These parameters were the APD quantum efficiency, from 35% to 40%; the preamplifier noise current spectral density, from 2 to 1.74 $pA/\sqrt{\text{Hz}}$; and the receiver signal voltage gain (or threshold scaling factor), from 1.32 to 1.28. The parameter values given in Table 2 are the revised values. The original values of the APD quantum efficiency and preamplifier noise density used in [2] were based on the manufacturer's minimum acceptable performance specification for the batch of detectors. The revised APD quantum efficiency and preamplifier noise density listed in Table 2 were the typical values reported by the manufacturer. The small adjustment in the receiver gain, 3% (0.26dB), is well within the tolerance of the circuit components used.

Figure 5 illustrates how the background light power can be determined from the false alarm rate and the threshold level, as in Eq.(1). This surface plot is used as a look up table in the MOLA ground data processing to obtain the background light power from the observed false alarm rate and the threshold level.

5 Measurement Precision and Accuracy

There are several factors that can affect the precision and accuracy of the MOLA passive radiometry measurements. These include the detector responsivity variation due to temperature, random fluctuation in the false alarm rate, uncertainty in the threshold level, and the slow drift in the receiver dark noise level and threshold voltage.

The receiver model and the parameter values described in the previous section are for near room-temperature conditions. However, during flight the detector temperature varies between 0°C and 40°C under different spacecraft operation conditions. The Si APD bias voltage is internally temperature compensated to maintain a fixed responsivity over this temperature range. As the temperature decreases, the APD quantum efficiency at 1064-nm laser wavelength decreases. The temperature compensation circuit then raises the APD gain to keep the overall responsivity constant to within ±10%. The increase in gain raises the false alarm rate. From measurements of similar devices, the temperature effects on the passive radiometry measurement can be corrected by a linear function as

$$P_0 = (0.66 + 0.0097 T_d) f(N_{fa}, v_{th}), \tag{16}$$

where T_d is the detector case temperature in $^\circ C$ and $f(N_{fa}, v_{th})$ refers to the function of background light power vs. false alarm rate and threshold at a nominal detector operating temperature ($35^\circ C$).

The detector case temperature in MOLA is not directly measured but has to be inferred from the detector assembly interface plate temperature contained in the telemetry data. The detector assembly is connected to the interface plate through the lens barrel. Because the Si APD responsivity is greater at higher temperature, an insulating fiberglass mounting fixture was used between the detector case and the lens barrel, allowing the detector case temperature to rise due to its own power dissipation. The detector subsystem can be modeled as a three-node cascade thermal system. Based on the fully-instrumented detector assembly prelaunch thermal test data, the APD case temperature, T_d, was 7.25°C higher than that of the detector lens barrel, T_m, and 12.5°C higher than that of the interface plate, T_i, at steady state in vacuum. Neglecting radiative losses, the steady-state temperatures obey Fourier's law of conduction,

$$Q = k_1(T_d - T_m) = k_2(T_m - T_i), \tag{17}$$

where $Q = 1.25$ W is the heat generated by the detector module, and k_1 and k_2 represent the thermal conductivities of the detector circuit board and mounting fixture, respectively.

The actual APD temperature in flight responds to changes in T_i with a significant delay due to the thermal inertias of the detector case c_d, the detector lens mount c_m, and the interface plate.

For the three node thermal system, the instantaneous temperatures are related by a coupled pair of differential equations:

$$\dot{T}_d = \frac{Q - k_1(T_d - T_m)}{c_d}, \tag{18}$$

$$\dot{T}_m = \frac{k_1(T_d - T_m) - k_2(T_m - T_i)}{c_m}, \tag{19}$$

where $\dot{T}$ denotes the time-derivative of temperature.

The response time delay constants estimated for this system are ~2400 s and ~450 s, comparable to the time scales of orbital changes in thermal environment. These time constants were also consistent with our observations in flight when MOLA experienced sudden temperature changes due to spacecraft operation. The instantaneous detector case temperature in response to the interface plate temperature is obtained by numerically integrating Eq.(17) through Eq.(19).

The detector dark noise varies with temperature and is automatically measured when the spacecraft is over the night side of Mars. For small changes in temperature, the effect can be approximated as a small offset in the effective detection threshold, a linear function of the detector case temperature. The effect can be compensated for by using an effective threshold, v_{eth}, in Eq.(15), as

$$v_{eth} = v_{th} - (a_0 + a_1 T_d), \tag{20}$$

with v_{th} given in Eq.(15). For Channel 2, the offset coefficients are estimated to be $a_0 = 3.60 \times 10^{-3}$ and $a_1 = 3.13 \times 10^{-5}$.

The amount of random error in the false alarm rate measurement can be estimated. We assume that the number of false alarms is a Poisson random variable with its variance equal to the mean. For MOLA's laser ranging operation, the false alarm rate had to be low. It was controlled at about 100 per second so that the probability of a false alarm within the 20-km nominal range gate interval (133 μs) was less than 1%. The standard deviation of the measurement error in the false alarm rate was, therefore, about 10%. For the enhanced radiometry mode operation, threshold level was lowered and controlled at about 10,000 per second, so that the random counting error was reduced to about 1%.

The uncertainty in the threshold level mainly comes from the inherent circuit noise at the comparator inputs, and the quantization error in digital-to-analog converter (ADC) output. The standard deviation of the inherent circuit noise was assumed to be 1 mV, which was typical for this type of circuit. The quantization error of the ADC may be modeled as a uniformly distributed random variable over the ADC step size. The ADC step size for MOLA threshold voltage generation is 1 mV. The standard deviation is $1/\sqrt{12}$ mV. The circuit noise and the quantization noise are independent of each other and the standard deviation is $\sqrt{1^2 + (1/\sqrt{12})^2} = 1.04\ mV$.

The standard deviation of the error in the background light power measurement due to the false alarm count fluctuation and circuit noise can be approximated as

$$\sigma_P = \left[\left(\frac{\partial P_o}{\partial y_{th}} \sigma_{y_{th}} \right)^2 + \left(\frac{\partial P_o}{\partial N_{fa}} \sigma_{N_{fa}} \right)^2 \right]^{1/2}, \tag{21}$$

where σ_{th} is the standard deviation of the threshold noise, and $\sigma_{N_{fa}}$ is the standard deviation of the number of false alarms, equal to the square root of the observed false alarm rate. The partial derivatives, $\partial P_o / \partial y_{th}$ and $\partial P_o / \partial N_{fa}$, can be obtained from the slope of the surface plot shown in Figure 5 along the horizontal and vertical axis, respectively. Figure 6 shows the resulting normalized radiometry measurement error, defined as the ratio of the standard deviation to the mean. It shows that the majority of the measurement data have a relative error <5%. Measurements over low to mid latitude region with higher than 1 nW background light power have a relative error <2%.

The errors in the radiometry measurement may be further reduced by averaging the results from some or all the four receiver channels. Although all the channels share the same detector as the signal source, the false alarm rates are obtained over different electrical bandwidths and at different effective threshold levels. This means that the threshold crossings for different channels are not entirely correlated, thus in principle the uncertainties in the radiometry measurement may be improved by averaging them. On the other hand, the channels with lower electrical bandwidth have poorer signal to noise ratios and are more susceptible to low-frequency circuit noise, such as $1/f$ noise and the spacecraft power supply noise. The overall passive radiometry measurements from MOLA were found to improve (i.e, less fluctuation in the along-track measurement) by averaging the results from Channels 1 and 2 but not Channels 3 and 4. Note that the threshold for Channel 1 was fixed near its maximum value during most of the laser ranging phase of the MOLA operation to reduce the ranging error and to minimize receiver saturation. Therefore, only Channel 2 passive radiometry measurements were available during that time.

There might also be long-term receiver degradation due to space radiation damage. The MGS radiation environment was estimated to be about 7 krad(Si) total dose per year during cruise and 6 krad(Si) per Mars year of operation behind 2.54 mm (100 mil) of aluminum shielding. The total dose at the detector which is the most sensitive to the radiation damage was much lower, a few krad(Si) or less, because of the shielding provided by the surrounding materials, such as the lenses and the telescope in front, the instrument chassis on the side, and the spacecraft on the back. The total doses for the sensitive electronics components should be similar or a few times higher, depending on position. In such a moderate radiation environment, the major effects to be considered are the increase in the detector dark current [14], the degradation of electrical circuits, and the darkening of the optics.

The Si APD dark noise increase due to space radiation is estimated to be 30 pA/krad(Si) [14], which is comparable to the APD dark current. As mentioned earlier, the total detector dark noise is monitored every orbit when MGS is on the dark side of Mars. The slow increase in dark current due to radiation damage could be compensated by adjusting the threshold bias as in Eq.(20), but the effects of space radiation on the electrical circuits and optics are believed to be negligible based on the instrument design, parts selection, and the preflight test data. The flight data shown in Figure 2 also confirmed that there was little change in the MOLA detector dark noise after five years in space and that the effect of space radiation is inconsequential.

6 Active and Passive Radiometry Measurements from Orbit

A sample of the MOLA threshold levels and the false alarm count rate for Channel 2 are plotted in Figure 7 as a function of the laser shot number for a complete orbit around Mars on June 29, 2001 (Orbit 20316) For this orbit, MOLA was in its normal laser ranging mode and Mars was near its northern autumnal equinox ($L_s \approx 180°$). Figure 8 shows the resultant Mars radiance factor based on these passive radiometry measurements. For comparison, the radiance factor obtained from the active radiometry measurement is also plotted. The atmosphere was cloudy during this time from a nascent global dust storm that the laser signals in the active radiometry measurement were substantially attenuated, while the backscattered sunlight from the passive radiometry measurement was relatively strong owing to backscattered sunlight.

During flight, the measured background light power onto the detector ranges from 0 to approximately 10 nW. In darkness, the effective noise of the measurement is about 0.01 nW in standard deviation per 0.125-second interval, measured over a 100 s baseline. At typical daytime background light power level, the noise level may be estimated from observations over relatively featureless terrain, and is approximately 0.025 nW at an average incident power of about 5 nW, or 0.5%, per 0.125 s. The noise is dominated by the counting statistics and is effectively white, so that the error may be reduced by averaging several successive measurements at the cost of coarser spatial resolution.

Figure 9 shows a Mars image constructed from the MOLA radiometry measurements over a period from March to June 1999. An image taken by the Hubble Space Telescope (HST) during the same period over a 61.1-nm optical bandwidth centered at 1042 nm [15] is also shown as a comparison. The MOLA measurements are similar to that of HST but reveal more features of the Mars surface. The difference between the absolute values of the two was about 60%. The HST measurements were taken at a solar phase angle between 2.7° and 10°, whereas the MOLA measurements are at phase angles greater than 23° owing to the 2 PM local time MGS orbit, which accounts in part for the greater reflectivity seen by HST. Another reason was that the HST image was taken at a different time and over a relatively short exposure time while the MOLA image were taken by scanning the planet over an 120-day period. Although the MOLA passive radiometry measurements were not absolutely calibrated in space, the receiver performance has been extremely stable since before launch (*cf* Figure 4).

Lastly, Figure 10 shows an image of the Mars mid latitude regions from the MOLA passive radiometry measurement data over three Martian years, from the commencement of the MGS mapping phase to December 2004. To demonstrate the MOLA measurement stability, the average radiance factors of two exceptionally bright and dark regions at Amazonis and Syrtis, 300x150 km in extent, are trended and plotted in Figure 10. The sudden shift in the radiance factor in the Amazonis region midway in the plot coincided with the change in the MGS viewing angle, superimposed on the effects of the planet-wide dust storm of 2001, and probably was due to the darkening effect of the greater phase angle. There was no apparent long-term downward trend, besides a seasonal variation, that was indicative of receiver responsivity degradation. Figure 10 illustrates that MOLA in its passive radiometry mode has provided a high-precision, near-infrared spectral map of Mars over the 1064 ± 1 nm spectral range. Monitoring of the temporal variations has the potential to study seasonal changes in the atmosphere and cryosphere of Mars [16, 17].

7 Acknowledgments

We would like to thank the guidance and support from the MOLA science team led by Dr. D. E. Smith. We would like to thank the MOLA instrument manager, R. B. Follas and the system engineer J. C. Smith for their guidance of the MOLA instrument development. We would like to thank the members of the MOLA electronics team, including R. L. Kasa, J. F. Cavanaugh, C. A. Long, J. N. Caldwell, A. T. Lukemire, R. B. Katz, G. C. Elman, J. R. Baker, J. F. McGarry, and P. L. Jester for their many expert contributions in the receiver design and testing. We thank Dr. J. F. Bell III for providing us the HST data used in Figure 9. In particular, we thank the MOLA software lead engineer J. B. Blair for the simple and yet flexible software design that

allowed MOLA to continue passive radiometry measurements without the on board clock oscillator during MGS extended mission.

References

[1] M. T. Zuber, D. E. Smith, S. C. Solomon, D. O. Muhleman, J. W. Head, J. B. Garvin, J. B. Abshire, and J. L. Bufton, 'The Mars Orbiter Laser Altimeter investigation,' *J. Geophys. Res.*, Vol. 97, pp. 7781-7797, 1992.

[2] J. B. Abshire, X. Sun, and R. S. Afzal, 'Mars Orbiter Laser Altimeter: Receiver model and performance analysis,' *Applied Optics*, Vol. 39, No. 15, pp. 2449-2460, May 2000.

[3] R. S. Afzal, 'Mars Observer Laser Altimeter: Laser Transmitter' *Appl. Opt.*, Vol. 33, pp. 3184-3188, 1994.

[4] L. Ramos-Izquierdo, J. L. Bufton, and P. Hayes, 'Optical system design and integration of the Mars Orbiter Laser Altimeter,' *Appl. Opt.*, Vol. 33, pp. 307-322, 1994.

[5] A. A. Albee, F. D. Palluconi, and R. E. Arvidson, 'Mars Global Surveyor Mission: Overview and status,' *Science*, Vol. 279, pp. 1671-1672, Mar. 1998.

[6] A. L. Albee, R. E. Arvidson, and F. D. Palluconi, 'Overview of the mars Global Surveyor mission,' *J. Geophys. Res.*, Vol. 106, pp. 23,291-23,316, 2001.

[7] D. E. Smith, M. T. Zuber, H. V. Frey, J. B. Garvin, J. W. Head, D. O. Muhleman, G. H. Pettengill, R. J. Phillips, S. C. Solomon, H. J. Zwally, W. B. Banerdt, T. C. Duxbury, M. P. Golombek, F. G. Lemoine, G. A. Neumann, D. D. Rowlands, O. Aharonson, P. G. Ford, A. B. Ivanov, P. J. McGovern, J. B. Abshire, R. S. Afzal, X. Sun 'Mars Orbiter Laser Altimeter (MOLA): Experiment summary after the first year of global mapping of Mars,' *Journal of Geophysical Research*, Vol. 106, pp. 23,689-23,722, 2001.

[8] C. Fröhlich, and J. Lean, 'Total solar irradiance variations: The construction of a composite and its comparison with models', in F. L. Deubner (ed.), IAU Symposium 185: *New Eyes to See Inside the Sun*

and Stars, Kluwer Academic Publ., Dortrecht, The Netherlands, pp. 89-102, 1998.

[9] J. S. Accetta and D. L. Shumaker, *The Infrared and Electro-Optical Systems Handbook*, SPIE, Environmental Research Institute of Michigan, Ann Arbor, 1993.

[10] A. B. Ivanov, and D. O. Muhleman, 'Opacity of the Martian atmosphere from Mars Orbiter Laser Altimeter (MOLA) observations,' *Geophys. Res. Lett.*, *25*, 4417–4420, 1998.

[11] B. Hapke, *Theory of Reflectance and Emittance Spectroscopy*, Cambridge University Press, New York, 1993, Ch.8.

[12] M. I. Skolnik, *Introduction to Radar Systems*, McGraw-Hill, New York, 1962.

[13] P. P. Webb, R. J. McIntyre, and J. Conradi, 'Property of avalanche photodiodes,' *RCA Review*, Vol. 35, pp. 234-278, June 1974

[14] X. Sun, D. Reusser, H. Dautet, and J. B. Abshire, 1997, 'Measurement of proton radiation damage of Si avalanche photodiodes,' *IEEE Trans Electon Devices*, Vol. 44, pp. 2160-2166, Dec 1997.

[15] J.F. Bell III, 'HST Studies of Mars', in *A Decade of Hubble Space Telescope Science*, M. Livio, K. Noll, and M. Stiavelli, editors, Cambridge University Press, pp. 1-24, 2003.

[16] M. T. Zuber and D. E. Smith, 'Observations of he seasonal polar icecaps of mars at 1064 nm,' *Third Mars Polar Science Conference*, Oct. 13-17, 2003, Alberta, CA.

[17] S. Byrne, M. T. Zuber, and G. A. Neumann, 'Martian residual-ice cap albedos from MOLA radiometry,' *Eos Trans. AGU, 85(47)*, Fall Meet. Suppl. Abstract P13A-0974, San Francisco, CA, Dec. 13-17, 2004.

Table 1: MGS Chronology and MOLA Measurement Configurations

Beginning Date	MGS Phase	MOLA measurements	Viewing angle	Radiometry resolution (along track)
7 Nov, 1996	Launch			
11 Sept. 1997	Orbit Insertion			
15 Sept. 1997	Aerobraking			
3 Mar. 1999	Mapping			
3 Mar. 1999		Laser ranging	0° (Nadir)	0.15 km dia spot
		& active radiometry	0° (Nadir)	at 0.3 km spacing
		passive radiometry	0° (Nadir)	0.34x3 km footprint
31 Jan. 2001	Extended Mission			
30 June 2001		(MOLA clock oscillator anomaly & investigations)		
10 Oct. 2001		Enhanced passive radiometry	18°	0.34x0.5 km

* Enhanced passive radiometry measurements continues to this date.

Table 2: MOLA Instrument Parameter Values Related to the Passive Radiometry Measurements

Symbol	Value	Description
λ	1064-nm	laser wavelength
A_{tel}	0.170 m^2	receiver telescope entrance aperture area
θ_{FOV}	0.850 mrad	receiver field of view (FWHM))
τ_{rcvr}	56.5%	receiver optics transmission
$\Delta\lambda$	2.0 nm	receiver optical bandwidth (FWHM)
η_d	40%	APD quantum efficiency at 1064-nm wavelength
G	120	average APD gain
k_{eff}	0.008	APD ionization coefficient ratio
I_{ds}	15 nA	APD surface dark current
I_{db}	80 pA	APD bulk dark current
N_{amp}	$(2pA/Hz^{1/2})^2$	preamplifier input noise density
R_{det}	1.26×10^8 V/W	detector assembly responsivity
a_{thre}	1.28	threshold scaling factor for Channel 2
BW_{3dB}	5.54 MHz	receiver noise bandwidth for Channels 2 (scaling factors and bandwidth for other channels can be found in [2]; those scaling factors may requires minor adjustments to give consistent results as those from Ch.2).

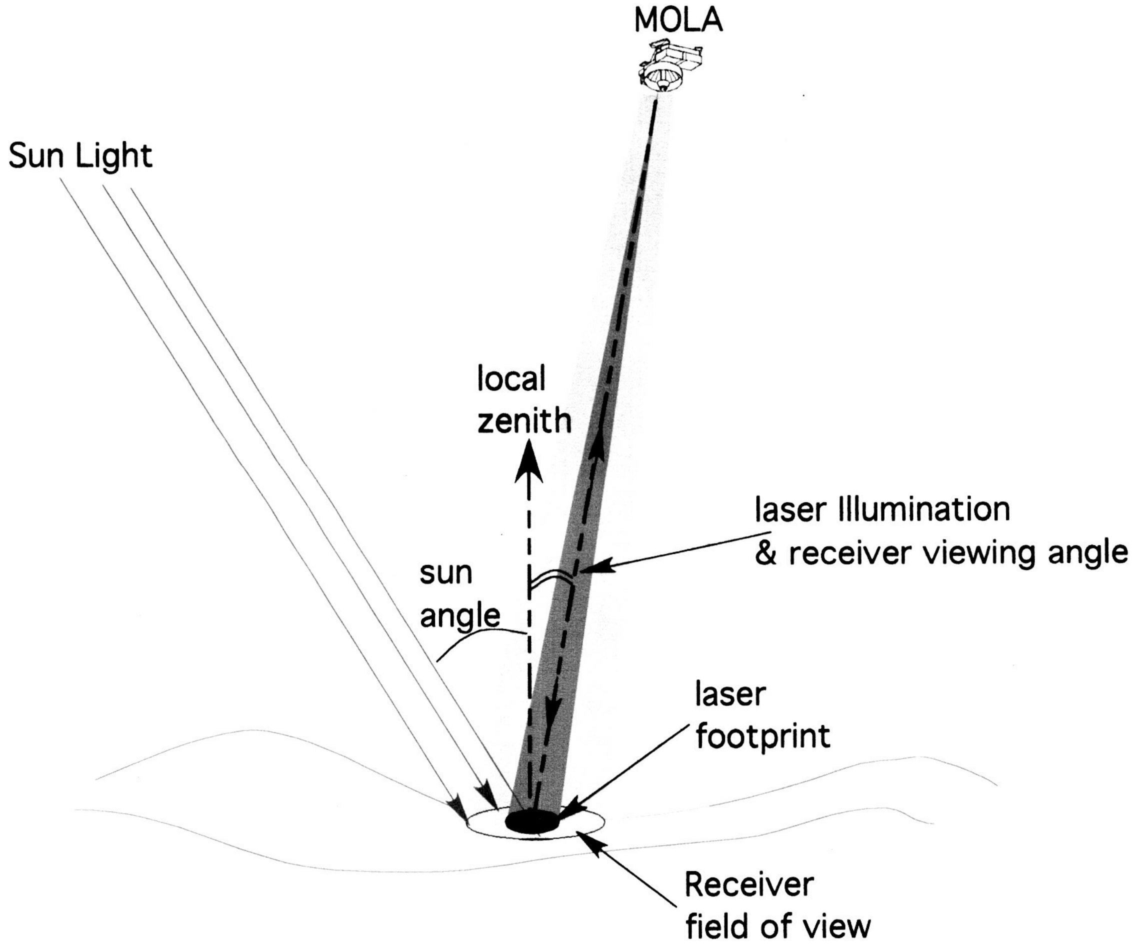

Figure 1. MOLA measurement configuration and geometry.

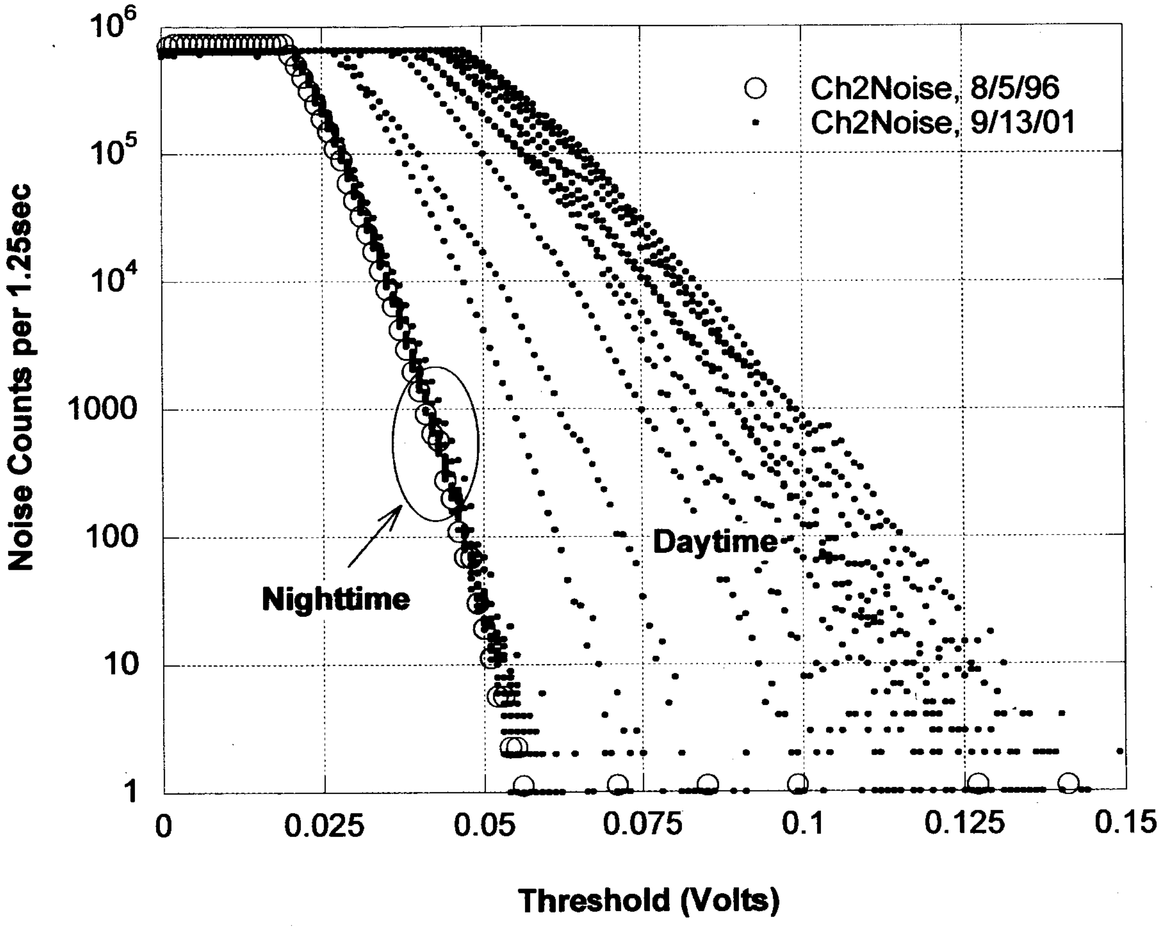

Figure 2. MOLA Channel 2 false alarm rate vs. threshold measured with MGS/MOLA in orbit around Mars in September 13, 2001. The measurements were taken as MGS flew from the dark side of Mars to the sunlit side. The prelaunch test data taken during August 5, 1996, is also plotted for comparison.

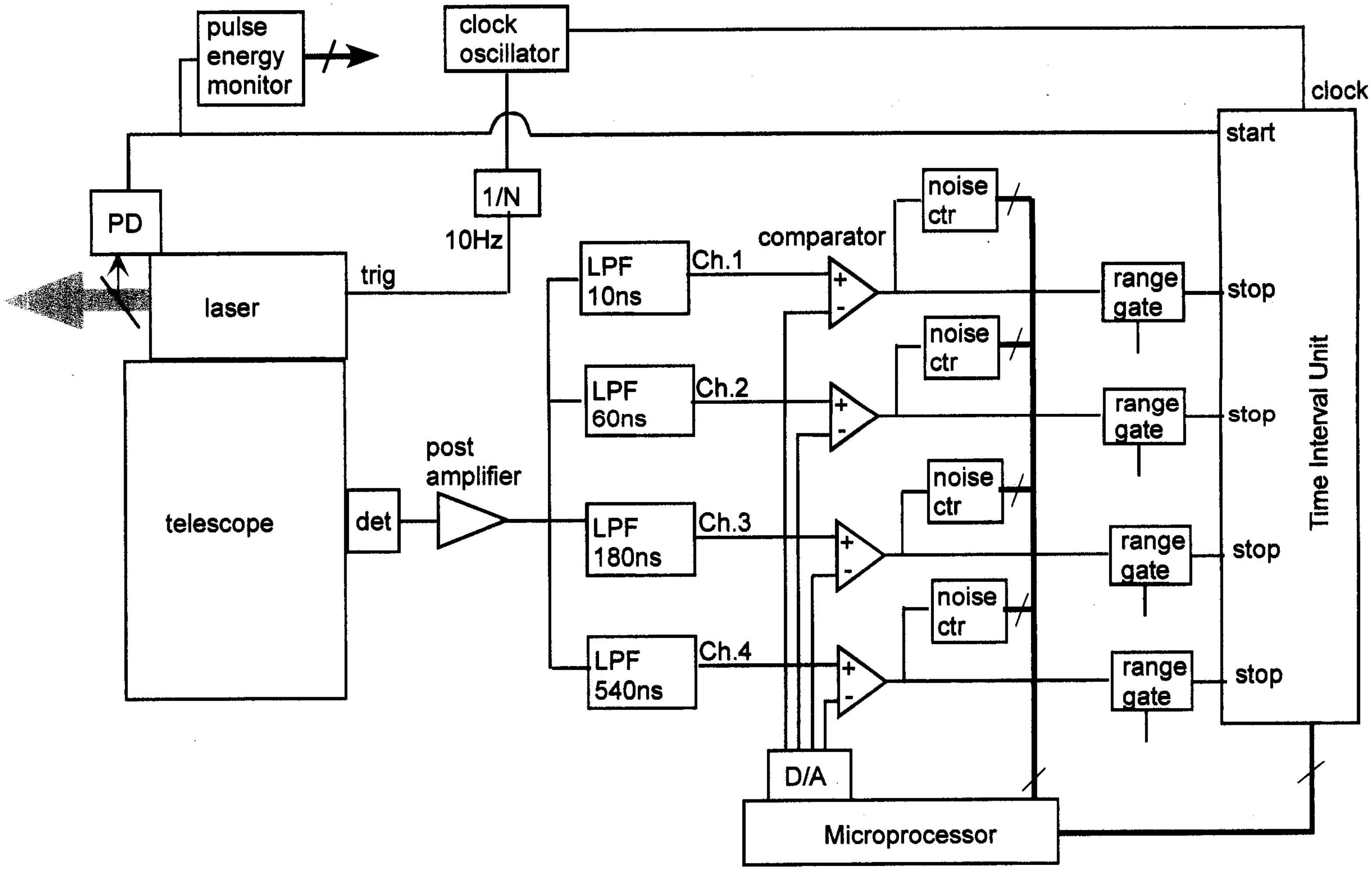

Figure 3. Simplified MOLA block diagram.

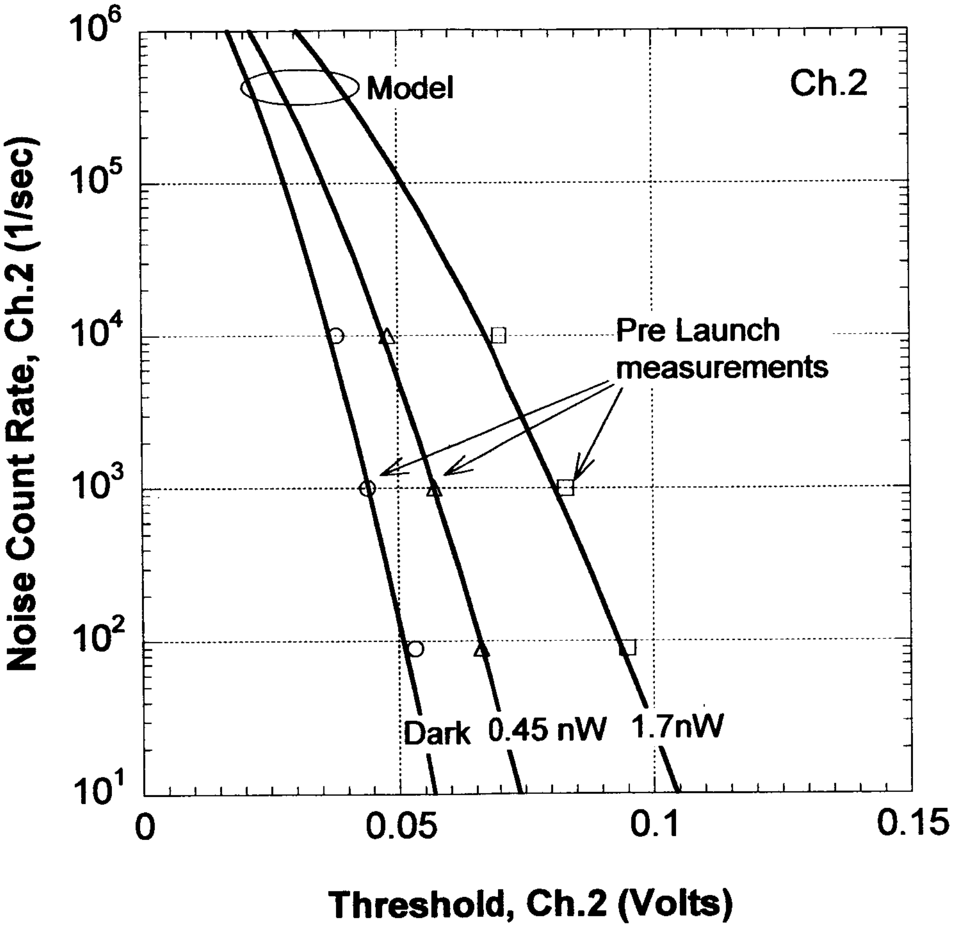

Figure 4. Comparison of the MOLA receiver model and the measured Channel 2 false alarm rate as a function of the threshold levels and the incident background light level.

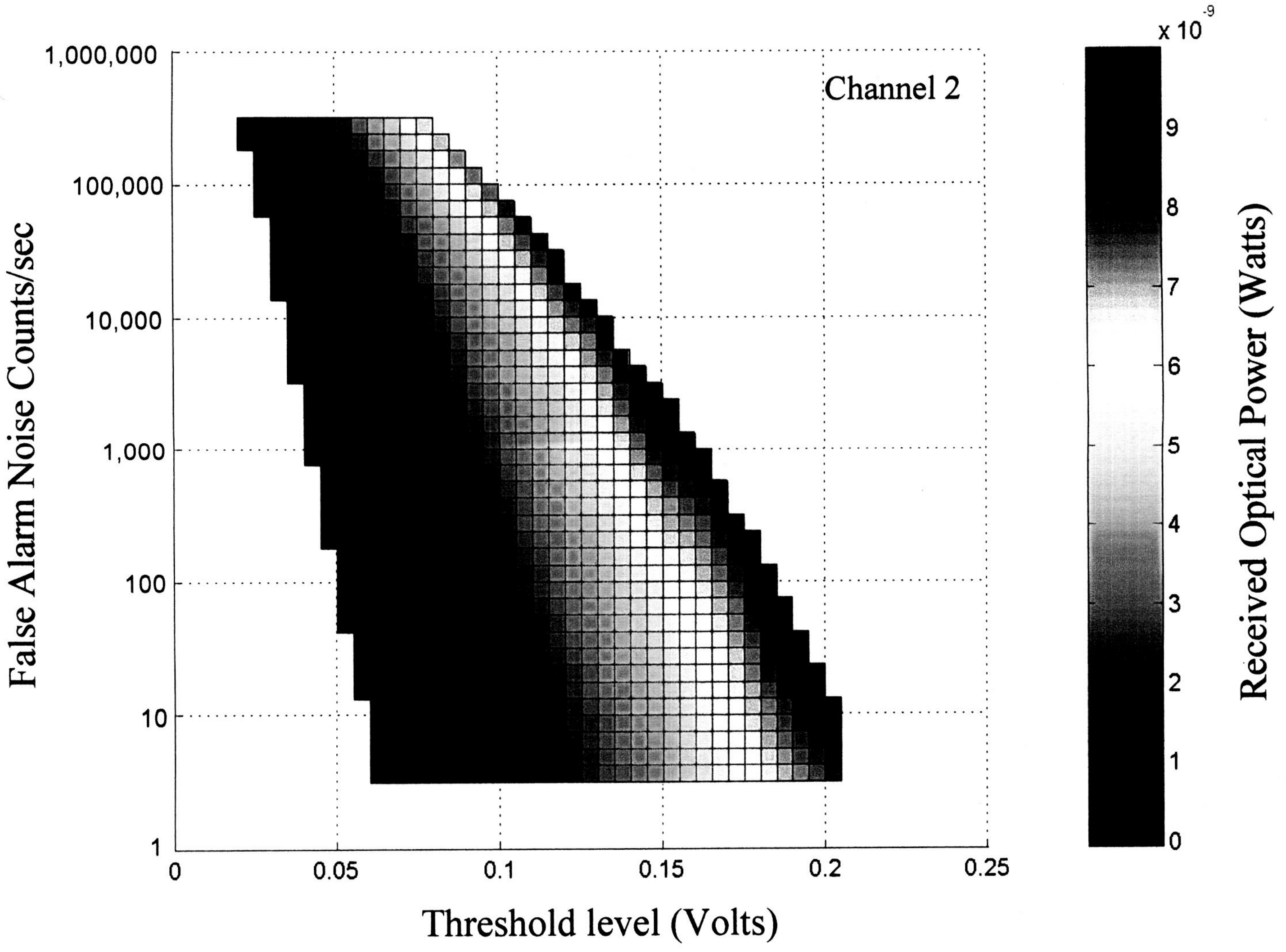

Figure 5. MOLA Channel 2 false alarm rate vs. threshold levels for background light ranging from dark to 10 nW.

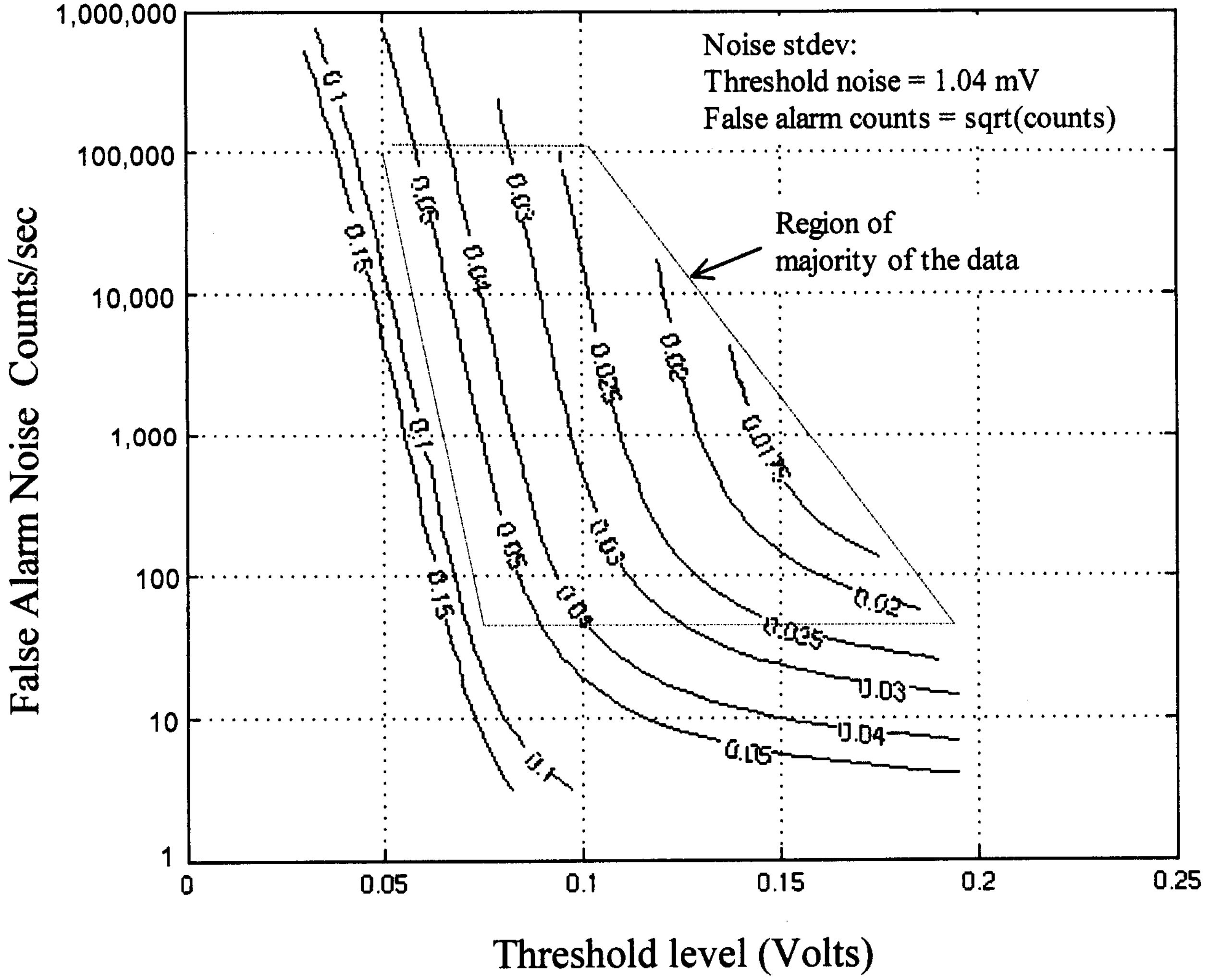

Figure 6. Relative error (stdev/mean) in MOLA radiometry measurements.

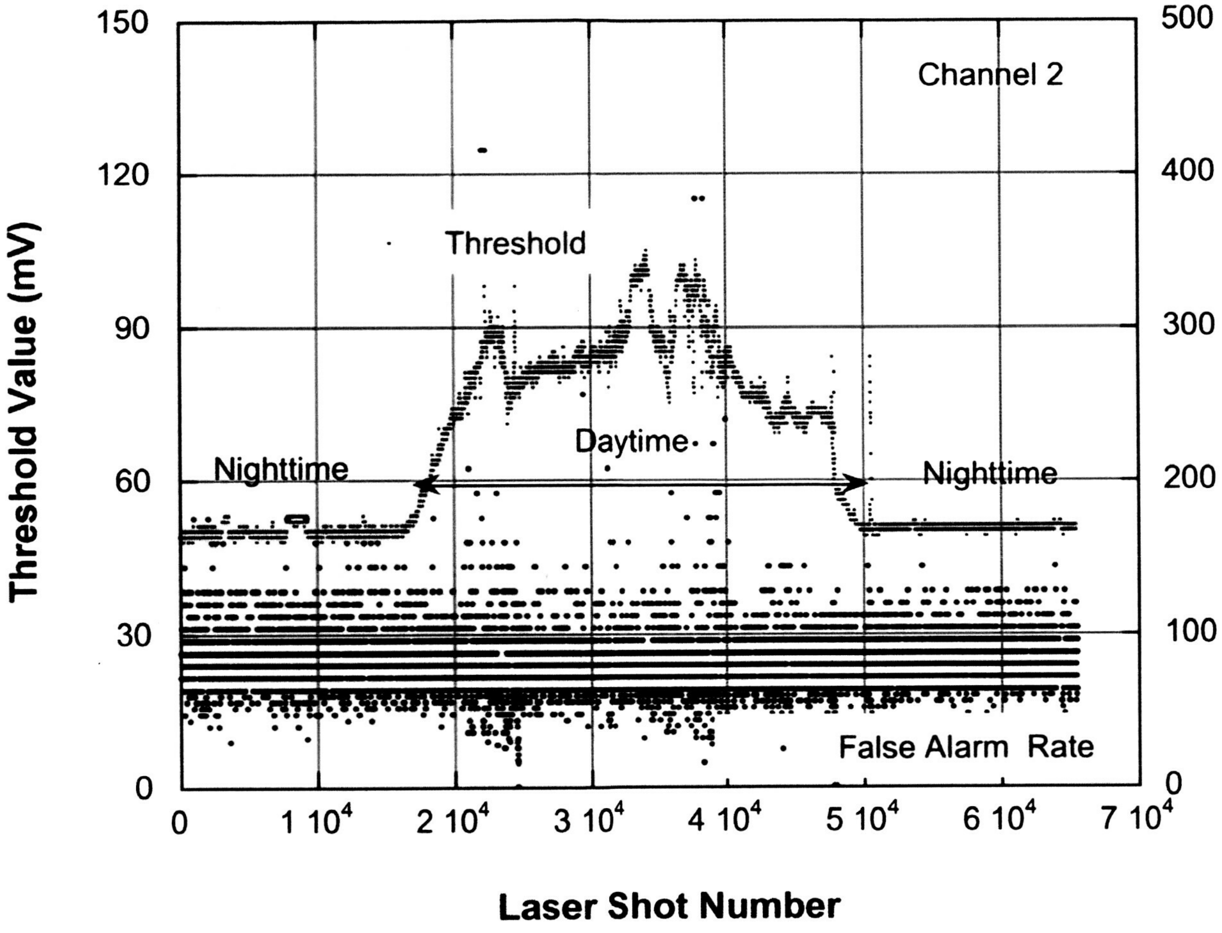

Figure 7. Sample MOLA threshold and false alarm count rates in normal ranging mode. Data taken on June 29, 2001 (orbit 20316).

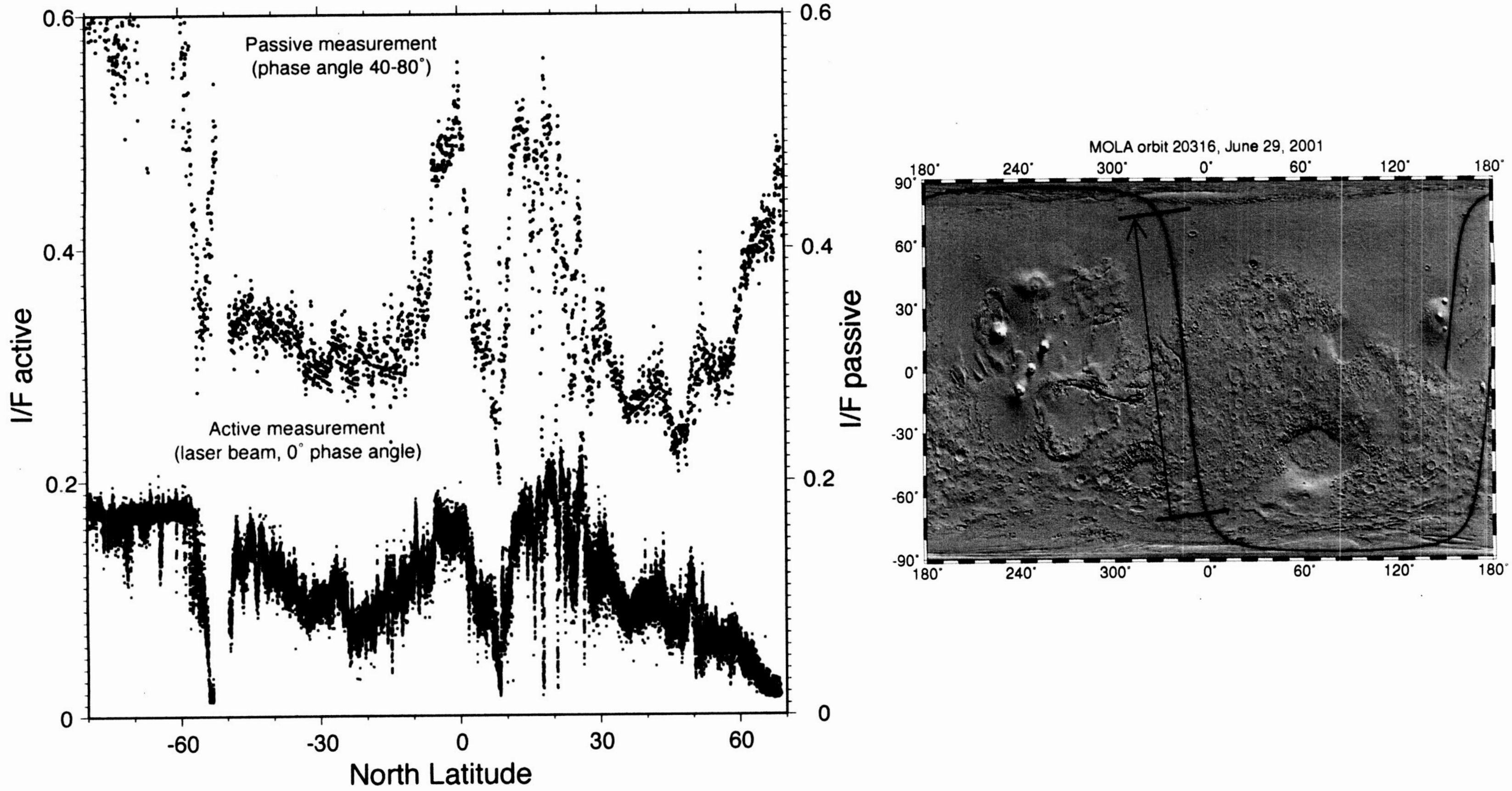

Figure 8. Mars radiance factor from MOLA Channel 2 passive radiometry measurement and active radiometry measurement for the day side of Orbit 20316 on 29 June 2001.

(a) HST 1042 nm

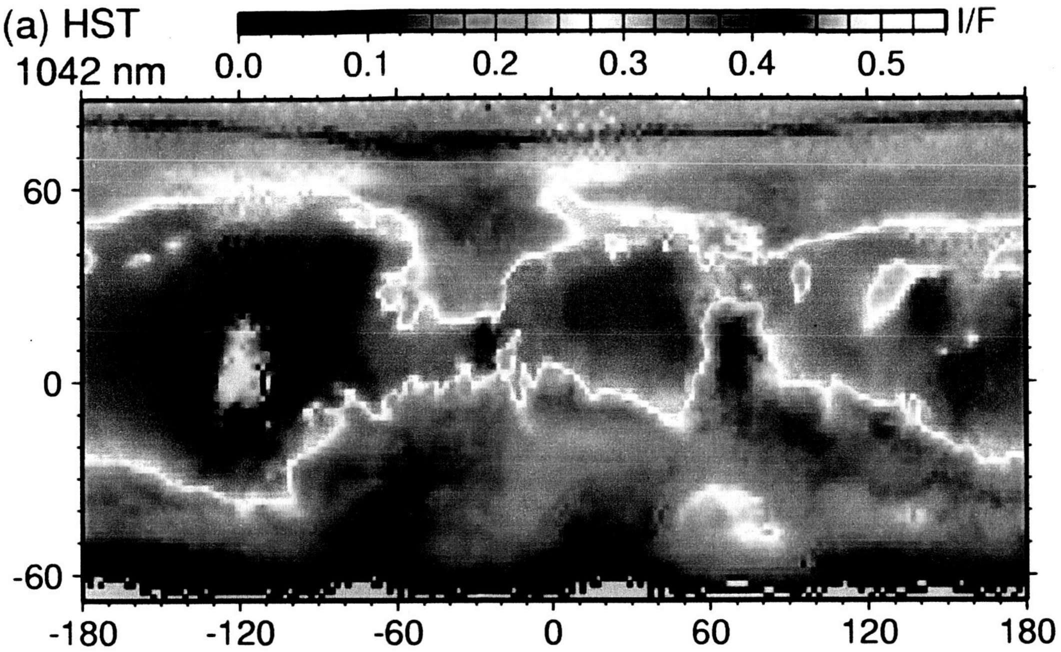

(b) MOLA 1064 nm

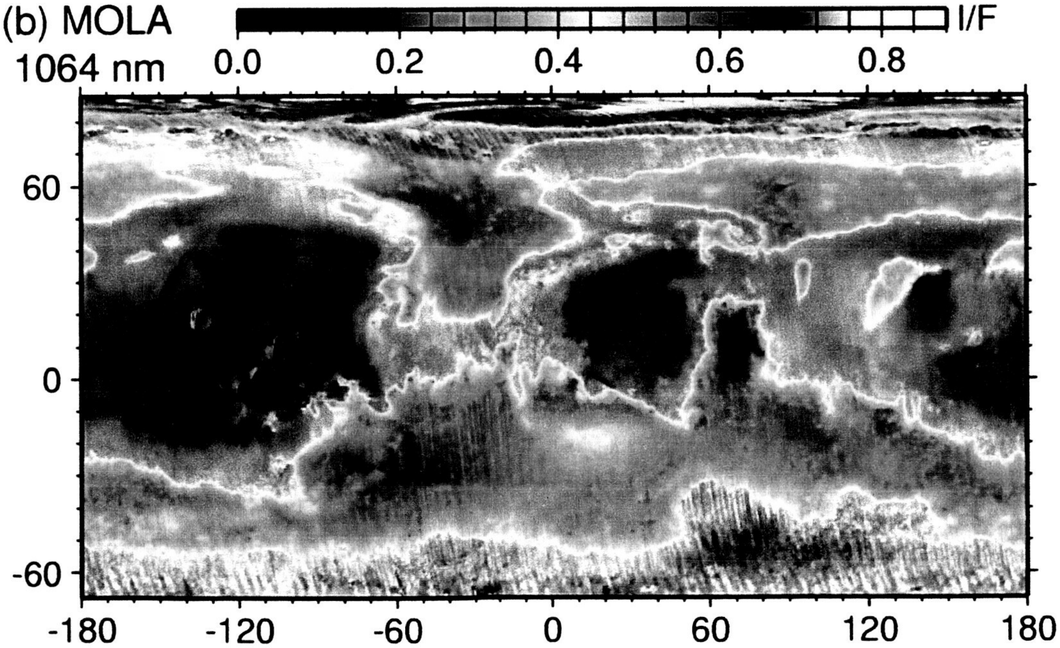

Figure 9. Images of Mars taken by the Hubble Space telescope (HST) (*a*) and by the MOLA passive radiometry measurement (*b*). The HST image was taken by the wide field camera (WFPC2) at 1.044±31 nm wavelength at a resolution of 20-30 km/pixel and a solar illumination angle of about 3 degrees. The MOLA measurement had an along-track spatial resolution of 3 km and orbit spacing of 3 km at the equator.

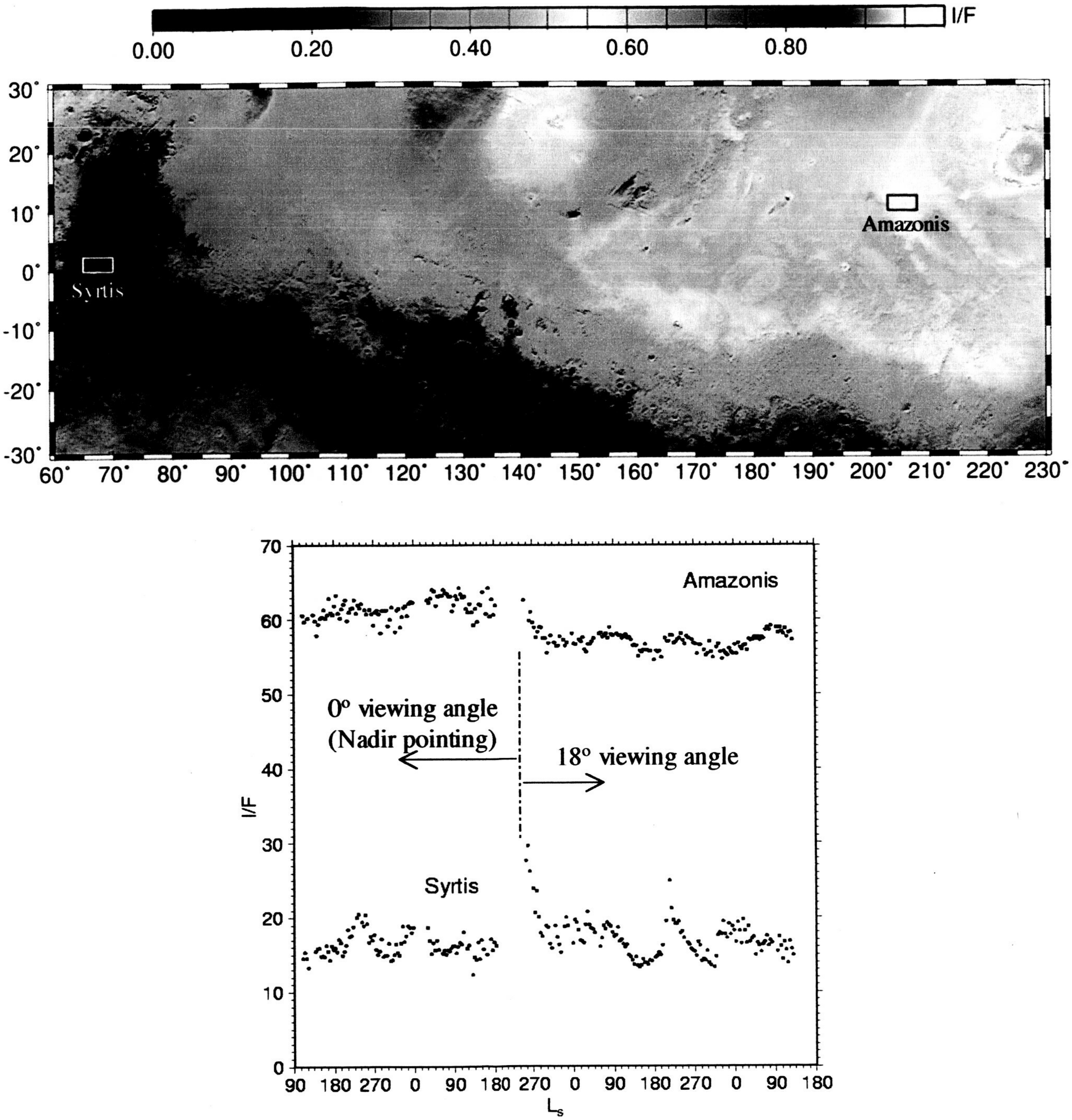

Figure 10. Image of Mars made from the MOLA passive radiometry measurements (top) and the average radiance factors vs. time in solar orbit positions from two 5° by 2.5° regions as a function of areocentric longitude of the sun, L_s, (bottom). The data were collected from the commencement of mapping phase in March 1999, $L_s = 104°$ ($L_s = 0°$ at northern hemisphere vernal equinox) to December 2004, $L_s = 12220°$ (or 140°).